Ab initio study of structural and electrical properties of $SrTiO_3$ dislocations

Daniel Gueckelhorn [1], Marivi Fernández-Serra [2,3], Cyrus E. Dreyer [2,4] and Andreas Ruediger [1,*]

[1] *Centre Énergie Matériaux Télécommunications, Institut National de la Recherche Scientifique, Varennes, Québec H2X 1E3, Canada*

[2] *Department of Physics and Astronomy, Stony Brook University, Stony Brook, New York 11794-3800, USA*

[3] *Institute for Advanced Computational Science, Stony Brook, New York 11794-3800, USA*

[4] *Center for Computational Quantum Physics, Flatiron Institute, 162 5th Avenue, New York, New York 10010, USA*

(Received 27 July 2026; accepted 28 October 2026; published 19 November 2026)

$SrTiO_3$ is a prototypical perovskite oxide with unique properties that have enabled its use in a wide range of applications, ranging from substrates to photovoltaics. Defects play a key role in the functional properties of $SrTiO_3$. In particular, dislocations, i.e., one-dimensional crystal imperfections, can drastically alter structural and electrical properties in their vicinity. In this work, we present a density functional theory study of the effects of dislocations on $SrTiO_3$. We find that dislocations introduce strong structural distortions with localized strain values reaching 0.17. As a consequence, nonpolar $SrTiO_3$ becomes polar, with polarization values up to 46 $\mu C/cm^2$, exceeding those of some polar perovskites. Dislocations also interrupt the periodic lattice arrangement, leading to phonon modes between 600 cm^{-1} and 1000 cm^{-1}. In terms of electrical properties, dislocations reduce the bandgap by smearing oxygen $2p$ and titanium $3d$ states. A Bader charge analysis reveals that free charge carriers accumulate in the heavily distorted regions around the dislocation cores. Overall, the system studied here provides a framework for understanding the key structural and electrical properties of dislocations.

DOI: 10.1103/dn2q-6714

I. INTRODUCTION

$SrTiO_3$ is one of the most prominent members of the perovskite material family. Properties of $SrTiO_3$ include high-temperature stability [1], a high dielectric constant [2], a metal-insulator transition with tunable conductivity [3], and a high refractive index [4]. Traditionally, the main application for $SrTiO_3$ is its use as a substrate for epitaxial growth of functional oxide thin films, including high-temperature superconductors [5], ferroelectrics [6], multiferroics [7], and two-dimensional electron gas heterostructures [8]. As a consequence of these properties, it can be found in capacitors as a high-k material [9], in memristors [10], or in optical setups [11]. Today, $SrTiO_3$ is in the spotlight for environmental applications, especially as a photocatalyst [12], and in perovskite solar cells as an electron transport layer [13].

In many of these cases, defects play a key role in the properties of $SrTiO_3$. These defects can be introduced on purpose, known as defect engineering, or are the unavoidable consequences of environmental factors. A common defect in $SrTiO_3$ is the dislocation.

Dislocations are one-dimensional crystal defects that describe interruptions in the periodic atomic arrangement. Dislocations may be of edge type, screw type, or mixed; this work focuses only on edge dislocations. The main reason is that edge dislocations are more common at higher temperatures [14]. Many experiments involve thermal annealing at temperatures in the range of several hundred degrees, often to generate vacancies [15] or to obtain atomically flat terrace structures [16]. Furthermore, edge dislocations are simpler to model and therefore easier to compare with existing work. These dislocations are created by inserting a half-plane into the crystal lattice, causing a localized interruption of the atomic stacking order. The strength of this distortion is described by the Burgers vector. Dislocations are abundant in every $SrTiO_3$ sample with densities between 10^6 cm^{-2} and 10^{11} cm^{-2} [17].

The presence of a dislocation locally alters a material's properties. Dislocations break the local symmetry [18], generating strain gradients that can induce polarization via flexoelectricity even in an otherwise nonpolar structure [19]. In $SrTiO_3$, dislocations can also act as conducting filaments in an otherwise insulating bulk phase after oxygen reduction [15], and these filaments can even be electrically switched [20]. More generally, dislocations are expected to play an important role in the physics of $SrTiO_3$, including the still unresolved mechanism of superconductivity, where local structural and electronic inhomogeneity may support localized superconducting regions [21].

This dislocation-centered picture is further strengthened by the strong coupling between dislocations and oxygen vacancies in $SrTiO_3$. Oxygen vacancies can drive a metal-insulator transition [15], modify electrical and optical properties [22], enhance photocatalytic activity and solar-cell efficiency [23], and introduce phonon modes [24]. While oxygen vacancies may form throughout $SrTiO_3$, both theory and experiment

*Contact author: andreas.ruediger@inrs.ca

Published by the American Physical Society under the terms of the Creative Commons Attribution 4.0 International license. Further distribution of this work must maintain attribution to the author(s) and the published article's title, journal citation, and DOI.

show that dislocations are preferential sites for vacancy accumulation [25–27]. While they act as centers for oxygen vacancy creation, they decrease the ionic conductivity, negatively impacting applications such as oxide fuel cells, batteries, and solar cells [28–30]. Together, these effects make them a natural focal point for understanding how structural defects reshape the material's electronic and functional properties.

Dislocations in $SrTiO_3$ have already been investigated experimentally and theoretically. The experimental work mainly focuses on the conductivity along these defects, as well as the induced lattice strain and its resulting polarization [18,25,26,31–35]. The theoretical work, mainly density functional theory (DFT) and molecular dynamics (MD) simulations, focuses on oxygen vacancy formation, oxygen diffusion, structural properties, and transport properties [18,25,27,29,30,36,37]. Calculations of electrical properties are limited to the density of states (DOS) and Bader analysis of a single dislocation structure [18,20]. Therefore, an in-depth comparison of the electrical properties among the different dislocation types is still lacking. Furthermore, due to the computational expense of calculations, some authors used simplified dislocation geometries with a trivial Burgers vector, which is closer to a vacancy structure than to an actual dislocation [20,25,36]. Thus, these results do not account for two main components of a dislocation: a stacking error within the lattice and the resulting strain gradient.

The objective of this paper is to provide a detailed overview of the structural and electrical properties of dislocations in cubic ($Pm\bar{3}m$) $SrTiO_3$ from DFT. We show that dislocations introduce strong local distortions, leading to large strain and the emergence of finite polarization in an otherwise nonpolar material. They also give rise to additional phonon modes in the high-frequency range, reflecting the broken periodicity and altered bonding environment around the dislocation core. In addition, the electronic structure is significantly modified, with a reduced bandgap and charge accumulation in the heavily distorted regions near the dislocation. Together, these results demonstrate that dislocations can profoundly affect both the structural and electronic properties of $SrTiO_3$ and provide a framework for future studies, including dopants, oxygen vacancies, free charge carriers, or spin-related effects. Even though the system of choice was $SrTiO_3$, these fundamental findings of the interplay between structural and electrical properties should expand beyond this single material to include other oxide materials such as MgO [38], TiO_2 [39], YSZ [40], or CeO_2 [41], as these materials show similar trends regarding oxygen vacancy formation energy and ionic conductivity in the presence of dislocations.

II. COMPUTATIONAL APPROACH

A. Computational parameters

The DFT + U calculations were performed with the SIESTA package [42]. For all calculations, the Perdew-Burke-Ernzerhof (PBE) functional [43], pseudopotentials from the open-source project PseudoDojo (v0.4.1, stringent) [44], a triple-zeta valence polarized (TZVP) basis set, a $6 \times 6 \times 6$ Monkhorst-Pack k grid [45] for the primitive cell, and a Hubbard correction term of $U = 4.45$ eV for titanium $3d$ orbitals were employed. This value delivered accurate results in previous $SrTiO_3$ DFT + U studies [46,47]. All geometries were optimized until the forces were below 0.04 Å/eV. These parameters lead to the calculated lattice constant $a_0 = 3.953$ Å. This value is slightly larger compared to the experimental value of 3.905 Å [48] and is a well-known effect of generalized gradient approximation (GGA) functionals, like PBE [49].

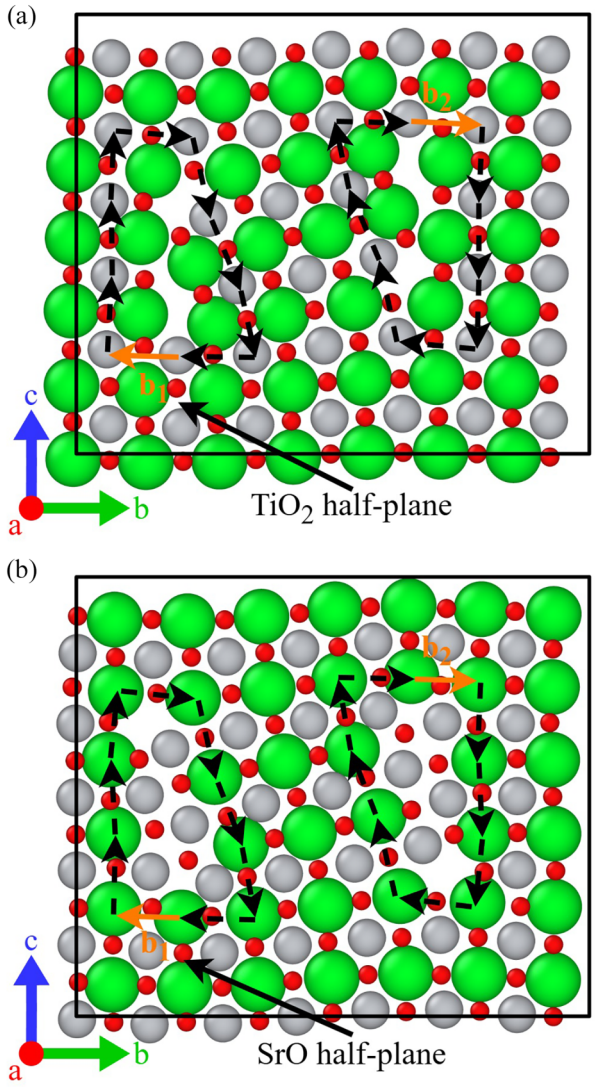


FIG. 1. Simulation geometry of a (a) SrO-type dislocation created by inserting a TiO_2 half-plane and a (b) TiO_2-type dislocation created by inserting a SrO half-plane into bulk $SrTiO_3$. Two opposing dislocations are needed to apply periodic boundary conditions. The dashed lines outline represent a Burgers circuit with the Burgers vectors $\mathbf{b}_1$ and $\mathbf{b}_2$ highlighted in orange.

B. Simulation geometry

The two possible edge dislocations for $SrTiO_3$ were created by inserting a SrO and a TiO_2 half-plane, respectively. For this purpose, a $1 \times 7 \times 6$ supercell, with a $6 \times 1 \times 1$ Monkhorst-Pack k grid, was modified, as shown in Fig. 1. To

TABLE I. Burgers vectors $\mathbf{b}_1$ and $\mathbf{b}_2$ for SrO- and TiO_2-type dislocations, in $1/a_0$.

Dislocation	$\mathbf{b}_1$	$\mathbf{b}_2$	$\|\mathbf{b}_1\|$	$\|\mathbf{b}_2\|$
SrO-type	(0.00, −0.98, 0.06)	(0.00, 0.98, −0.07)	0.98	0.99
TiO_2-type	(0.00, −0.94, 0.10)	(0.00, 0.94, −0.10)	0.95	0.95

enable periodic arrangement in all directions, two opposing dislocations had to be used to cancel out the resulting stacking error within the crystal lattice. This arrangement leads to a continuous dislocation along the a axis. A vacuum of any kind was not employed, as we assume the dislocations are deep enough in the bulk and are not susceptible to external influence. When calculating the Burgers vectors for both dislocation types, we can see they cancel each other out nearly completely for both structures, with vector norms very close to the expected value of a_0, as summarized in Table I. Inserting a TiO_2 half-plane creates a SrO-terminated dislocation with 206 atoms ($Sr_{43}Ti_{40}O_{123}$); inserting a SrO half-plane creates a TiO_2-terminated dislocation with 209 atoms ($Sr_{40}Ti_{43}O_{126}$). Throughout the work, we will address the SrO-terminated dislocation as SrO-type dislocation and the TiO_2-terminated dislocation as TiO_2-type dislocation, respectively.

C. Calculation of phonon density of states

To calculate the phonon density of states (PhDOS), the force-constant matrix was obtained using the finite-displacement method, in which each atom in the simulation cell was displaced by 0.04 Bohr along the positive and negative Cartesian directions. Longitudinal-transverse optical (LO-TO) splitting was not included, as its evaluation requires the calculation of Born effective charges and the dielectric tensor, which was beyond the scope of these finite-displacement calculations. To enable direct comparison with pristine $SrTiO_3$ bulk, a $1 \times 7 \times 6$ $SrTiO_3$ bulk supercell was employed, reproducing the same Brillouin-zone folding effects and any supercell-induced artifacts. This approach enables evaluation of differences rather than absolute values.

D. Calculation of atomic strain

To quantify the structural distortion around the dislocation, we use a method based on the work of Robinson *et al.* [50]. Hereby, the TiO_6 octahedra are used as a measure of distortion. The total strain is derived from a combination of three independent factors: longitudinal strain ϵ_{long}, transverse strain ϵ_{trans}, and B-site off centering ϵ_{off}. A direct mapping between the defect and a reference structure is not feasible here due to the varying chemical environment. In order to prevent arbitrarily large strain values due to potential missing oxygen atoms, strain is only calculated if six oxygen atoms within a radius of 3 Å around the titanium atom are present.

The longitudinal component depends on the quadratic elongation λ, which captures changes in Ti-O bond lengths relative to a perfect octahedron in pristine $SrTiO_3$. This metric is defined as

$$\lambda = \frac{1}{6}\sum_{i=1}^{6}\left(\frac{l_i}{l_0}\right)^2, \tag{1}$$

where l_i represents the bond length between the central Ti atom and its ith oxygen neighbor, and l_0 is the reference length equal to $a_0/2$. An ideal octahedron corresponds to $\lambda = 1$. From this, ϵ_{long} is determined by

$$\epsilon_{\text{long}} = \lambda - 1. \tag{2}$$

To account for the transverse contribution, we utilize the bond angle variance σ^2. This parameter measures angular deviations in the O-Ti-O geometry between the defect and the pristine reference structure:

$$\epsilon_{\text{trans}} = \sigma^2 = \frac{1}{11}\sum_{i=1}^{12}\left(\theta_i - \frac{\pi}{2}\right)^2. \tag{3}$$

In this expression, θ_i represents the ith cisangle within the O-Ti-O cluster with the reference angle of $\frac{\pi}{2}$.

The B-site off centering represents the shift between the central titanium position $\mathbf{R}_{\text{Ti}}$ and the geometric center of the oxygen cage $\mathbf{R}_{\text{centroid,O}}$. The centroid position is defined by

$$\mathbf{R}_{\text{centroid,O}} = \frac{1}{6}\sum_{i=1}^{6}\mathbf{R}_{\text{O}_i}, \tag{4}$$

where $\mathbf{R}_{\text{O}_i}$ denotes the coordinates of the surrounding oxygen atoms. The resulting off-centering strain is given by

$$\epsilon_{\text{off}} = \frac{\|\mathbf{R}_{\text{Ti}} - \mathbf{R}_{\text{centroid,O}}\|}{l_0}. \tag{5}$$

Finally, the total scalar strain ϵ_{total} is calculated using the Euclidean norm of these three contributions:

$$\epsilon_{\text{total}} = \sqrt{\epsilon_{\text{long}}^2 + \epsilon_{\text{trans}}^2 + \epsilon_{\text{off}}^2}. \tag{6}$$

E. Calculation of localized polarization

To calculate the local polarization, we first determine the local dipole $\mathbf{p}$ using the following equation [51]:

$$\mathbf{p} = \mathbf{Z}^*_{\text{Ti}} \cdot \mathbf{d}_{\text{Ti}} + \frac{1}{2}\sum_{i=1}^{6}\mathbf{Z}^*_{\text{O,mean}} \cdot \mathbf{d}_{\text{O}_i}, \tag{7}$$

where $\mathbf{Z}^*$ is the Born effective charge of the respective element and $\mathbf{d}$ is the displacement vector between the octahedral center $\mathbf{R}_{\text{centroid,Sr}}$, defined by the strontium atoms

$$\mathbf{R}_{\text{centroid,Sr}} = \frac{1}{8}\sum_{i=1}^{8}\mathbf{R}_{\text{Sr}_i} \tag{8}$$

and the actual atomic coordinates. The downside of using a geometric origin based on strontium atoms is that their contribution to the polarization vanishes. However, this is the best trade off to keep the overall systematic error minimal, since strontium atoms move less than titanium and oxygen atoms due to their size and should therefore contribute the least to the total polarization. Similar to the strain calculation, we implemented cutoff radii to ensure realistic polarization values. Around the titanium atom, eight strontium atoms within a radius of 4 Å and six oxygen atoms within 3 Å must be present to proceed with the calculation. The Born charges, as shown in Table II, are obtained from a pristine, primitive $SrTiO_3$ cell. For oxygen atoms, the effective charges are assigned

TABLE II. Born effective charges Z^* in cubic ($Pm\bar{3}m$) $SrTiO_3$, in e.

Ion	Z^*_{xx}	Z^*_{yy}	Z^*_{zz}
Sr	2.03	2.03	2.03
Ti	6.93	6.93	6.93
O1	−1.66	−1.66	−5.65
O2	−1.66	−5.65	−1.66
O3	−5.65	−1.66	−1.66

in a direction-dependent manner by identifying the principal axis closest to each oxygen relative to the central titanium atom and applying the corresponding tensor component. The 1/2 scaling factor for oxygen accounts for the fact that these atoms are shared between neighboring cells. The resulting local polarization **P** is then calculated by dividing the dipole **p** by the unit cell volume Ω:

$$\mathbf{P} = \frac{\mathbf{p}}{\Omega}. \tag{9}$$

The resulting polarization P_{total} is obtain via the Euclidean norm

$$P_{\text{total}} = \|\mathbf{P}\|. \tag{10}$$

III. RESULTS AND DISCUSSION

A. Structural properties

The first structural property we will address is the induced strain near the dislocation. As shown in Fig. 2(a), the SrO-type dislocation shows maximum strain values of 0.17 with average strains of 0.05. The regions with the highest strain are located directly along the dislocation core. For the TiO_2-type dislocation, depicted in Fig. 2(b), strain values up to 0.13 with average values of 0.06 can be observed. Similar to the SrO-type dislocation, the areas with the highest strains are found directly at the dislocation core. A possible reason why the TiO_2-type dislocation has lower strains compared to the SrO-type dislocation is that titanium atoms are more mobile than strontium atoms and can therefore move more freely and can compensate for emerging high-strain areas. An overview of statistical values of ϵ_{total} is given in Table III. When comparing strain values reported in previous work, it is important to account for differences in structure, strain definition, and the specific strain components reported. In theoretical work, an MD study reported strain values of around 0.03 [25]. In that case, strain was defined as the lattice difference between two strontium atoms in the distorted structure relative to pristine $SrTiO_3$. Moreover, the structure did not contain a stacking fault; instead, the removal of a $SrTiO_3$ cell strip produced a geometry more similar to a vacancylike defect. The use of strontium atoms as a reference, which have low mobility,

TABLE III. Descriptive statistics of ϵ_{total} for SrO- and TiO_2-type dislocations.

Dislocation	Average	Median	Min	Max
SrO-type	0.052	0.042	0.006	0.171
TiO_2-type	0.058	0.055	0.015	0.127

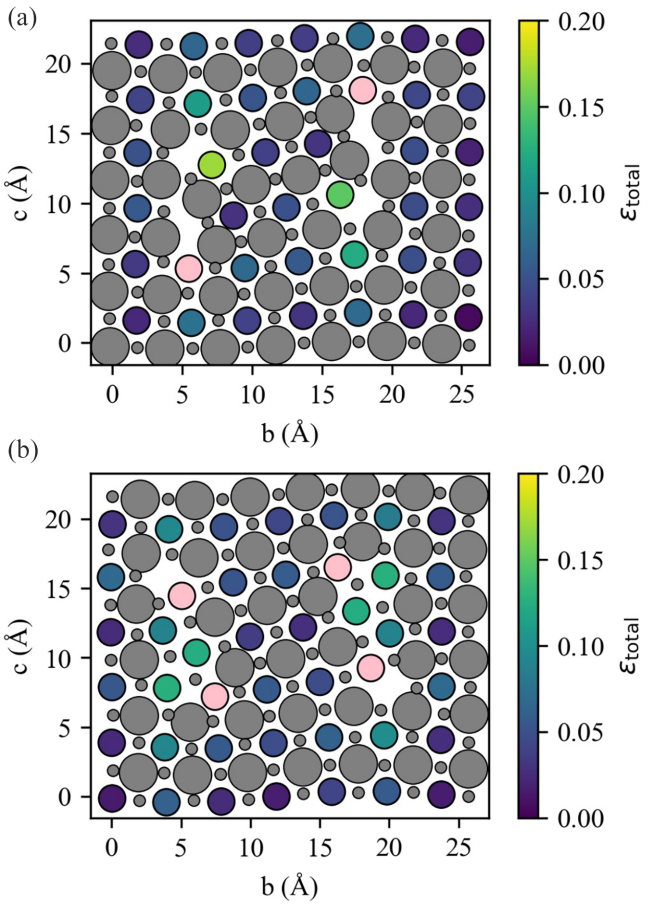


FIG. 2. Strain maps of the (a) SrO-type dislocation and the (b) TiO_2-type dislocation. To improve the overview, only the central Ti atoms were highlighted instead of the complete TiO_6 octahedra. For atoms marked in pink, no strain value could be calculated.

together with the symmetric geometry, likely contributes to the comparatively low strain values. A DFT study with a geometry similar to ours reported strain components of up to 0.09 [18]. Experimental studies reported maximum strain components of 0.1 [31,34], while another work found values as high as 0.6 [32]. This larger value is likely related to the different methodology used to evaluate strain in systems with too few neighboring atoms for a conventional local strain analysis. Taken together, these comparisons indicate that the absolute strain values are highly method dependent, but the values obtained here are consistent with the range reported for similarly distorted $SrTiO_3$ defect structures.

As a result of this strain, nonpolar cubic $SrTiO_3$ exhibits strong, localized polarization. This effect, known as flexoelectricity, arises when strain gradients induce polarization. It was experimentally demonstrated for $SrTiO_3$ [19]. For the SrO-type dislocation shown in Fig. 3(a), the total polarization reaches 37 $\mu C/cm^2$, with an average value of 18 $\mu C/cm^2$. Examining the Cartesian components of **P**, the average values lie between −1.1 $\mu C/cm^2$ and 2.3 $\mu C/cm^2$, suggesting that regions with opposite polarization largely compensate each other. Comparing the minimum and maximum polarization components in Table IV, the total polarization is dominated by the *b* and *c* directions, with negligible contribution along *a*.

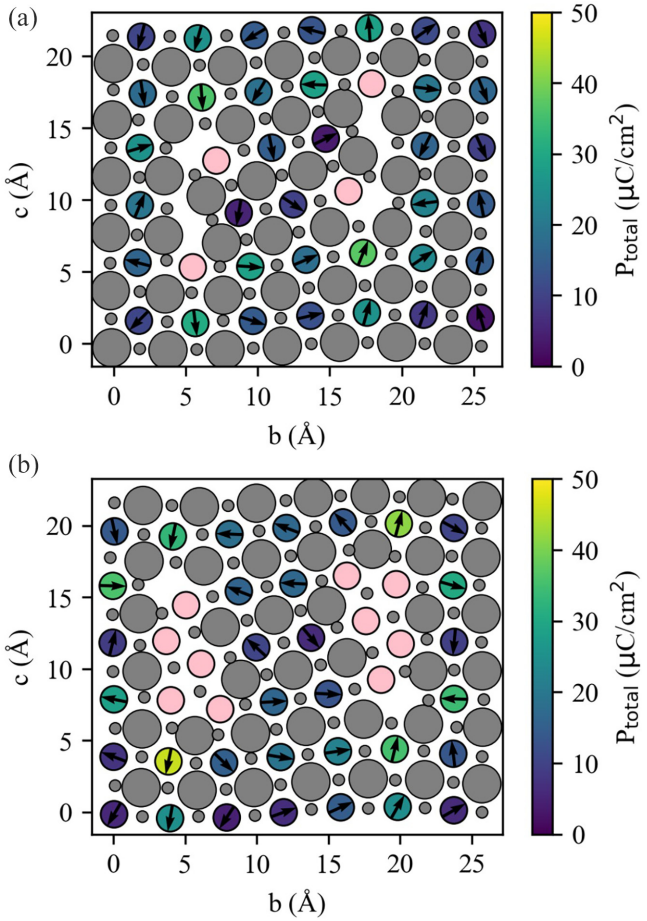


FIG. 3. Polarization maps of the (a) SrO-type dislocation and the (b) TiO_2-type dislocation. To improve the overview, only the central Ti atoms were highlighted instead of the complete TiO_6 octahedra. Arrows represent the direction of the polarization. For atoms marked in pink, no polarization value could be calculated.

For the TiO_2-terminated case, shown in Fig. 3(b), we find values up to 46 μC/cm^2, with an average total polarization of 19 μC/cm^2. Similar to the SrO-type dislocation, the average polarization along the different directions nearly vanishes, with values between 0.07 μC/cm^2 and 1.21 μC/cm^2. The polarization is also largely oriented along the *b* and *c* directions, as shown in Table V.

These maximum total polarization values for both dislocation types exceed the polarization of polar tetragonal $BaTiO_3$, which is about 25 μC/cm^2 [52]. However, in both cases, the opposing dislocation-induced regions cancel the total polarization. In a real $SrTiO_3$ crystal, this would cause the material

TABLE IV. Descriptive statistics of P_{total} and the Cartesian components P_a, P_b, P_c of **P** for SrO-type dislocations, in μC/cm^2.

	Average	Median	Min	Max
P_{total}	17.55	16.03	2.78	37.20
P_a	−1.10	−1.12	−1.29	−0.83
P_b	2.31	2.97	−28.56	28.75
P_c	−1.09	−2.27	−35.90	34.41

TABLE V. Descriptive statistics of P_{total} and the Cartesian components P_a, P_b, P_c of **P** for TiO_2-type dislocations, in μC/cm^2.

	Average	Median	Min	Max
P_{total}	18.78	15.86	4.67	45.82
P_a	0.07	0.03	−3.74	3.86
P_b	1.21	2.03	−34.47	35.73
P_c	0.23	0.97	−44.83	40.10

to remain nonpolar on a macroscopic scale, independent of the dislocation density, assuming a homogeneous distribution of dislocations. Similar to the strain distribution, the regions with high polarization are located directly along the dislocation cores. Experimental work reports mean polarization values of 28 μC/cm^2 with maximal values of 45 μC/cm^2 [31,32]. While our reported average polarization is somewhat smaller, the maximum polarization is in excellent agreement with these experimental results.

Dislocations also introduce other phonon modes. Figure 4 shows the calculated PhDOS of $SrTiO_3$ bulk and two

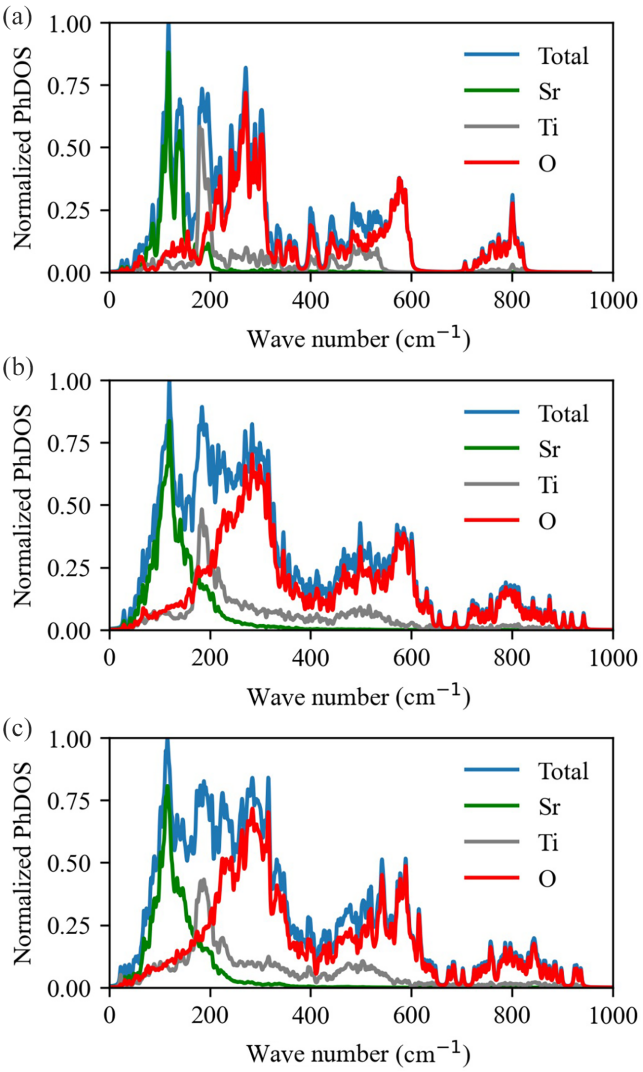


FIG. 4. Phonon density of states of the (a) $SrTiO_3$ bulk, (b) SrO-type dislocation, and (c) TiO_2-type dislocation.

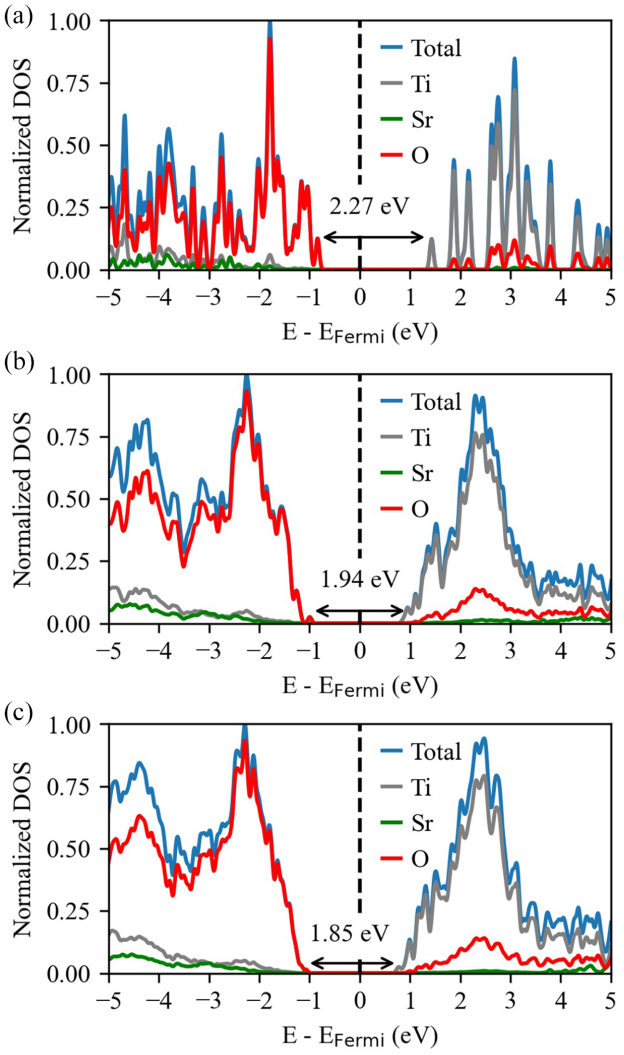


FIG. 5. Density of states of the (a) $SrTiO_3$ bulk, (b) SrO-type dislocation, and (c) TiO_2-type dislocation.

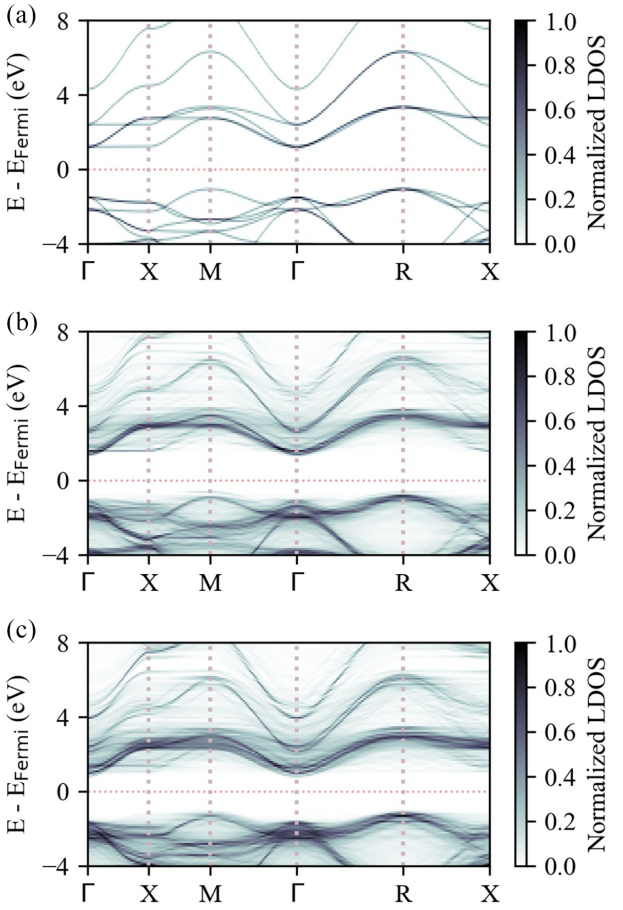


FIG. 6. Unfolded band structure of the (a) $SrTiO_3$ bulk, (b) SrO-type dislocation, and (c) TiO_2-type dislocation.

dislocation structures. The two dislocation structures show only minor, almost indistinguishable differences. Between 0 cm^{-1} and 600 cm^{-1}, all three PhDOS have a similar shape. Dislocations exhibit a wider range of states in this interval, but the overall shape remains the same. Between 600 cm^{-1} and 1000 cm^{-1} in the dislocation PhDOS, more phonon modes appear. These modes are driven mainly by oxygen atoms, with minor contributions from titanium. A previous Raman study of oxygen-reduced $SrTiO_3$ reported additional peaks between 650 cm^{-1} and 850 cm^{-1} with increased annealing duration [24]. This is in good agreement with our presented calculations. One possible explanation is that $SrTiO_3$ dislocations and oxygen vacancies can exhibit similar phonon signatures because both create a locally distorted bonding environment. Since dislocations are preferred nucleation sites for oxygen vacancies [15,25], oxygen reduction may enhance these defect-related vibrational modes and thereby strengthen the Raman signal. As a result, some of the observed Raman peaks may originate from dislocations rather than from oxygen vacancies alone. These results could therefore help identify dislocations in materials through nondestructive Raman measurements. Additionally, such defect-induced phonons could modify local electron-phonon interactions, potentially stabilizing a superconducting state as previously reported [53].

B. Electrical properties

Regarding the electrical properties, we start with the DOS analysis. The bandgap of the $SrTiO_3$ bulk with 2.27 eV is underestimated compared to the experimental value of 3.25 eV [54]. This is another well-known phenomenon of GGA potentials [55]. Both dislocation types have a reduced bandgap compared to the bulk phase, with 1.94 eV for the SrO-type dislocation and 1.85 eV for the TiO_2-type dislocation, as shown in Fig. 5. This reduction in both cases originates from the smearing of oxygen $2p$ and titanium $3d$ states sitting at the band edges due to an altered bonding environment along dislocations. This highlights that, even in the SrO-type dislocation, the electronic structure remains dominated by oxygen and titanium atoms, with strontium playing no significant role.

More insights can be extracted from the band structure. In order to be able to compare pristine bulk $SrTiO_3$ to the dislocations, the band structures were generated via band unfolding as described by Mayo *et al.* [56]. The unfolded bands are shown in Fig. 6 for pristine bulk $SrTiO_3$ and the two dislocation structures. The most prominent difference is the smearing of the dislocation band structures. This indicates an

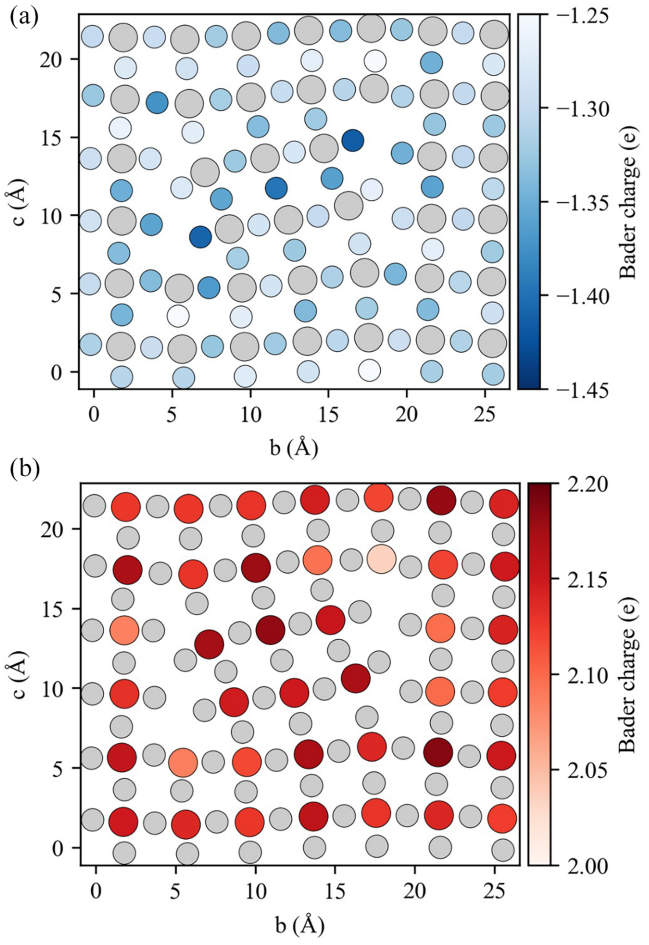


FIG. 7. Bader charges of the SrO-terminated dislocation with highlighted (a) oxygen and (b) titanium atoms.

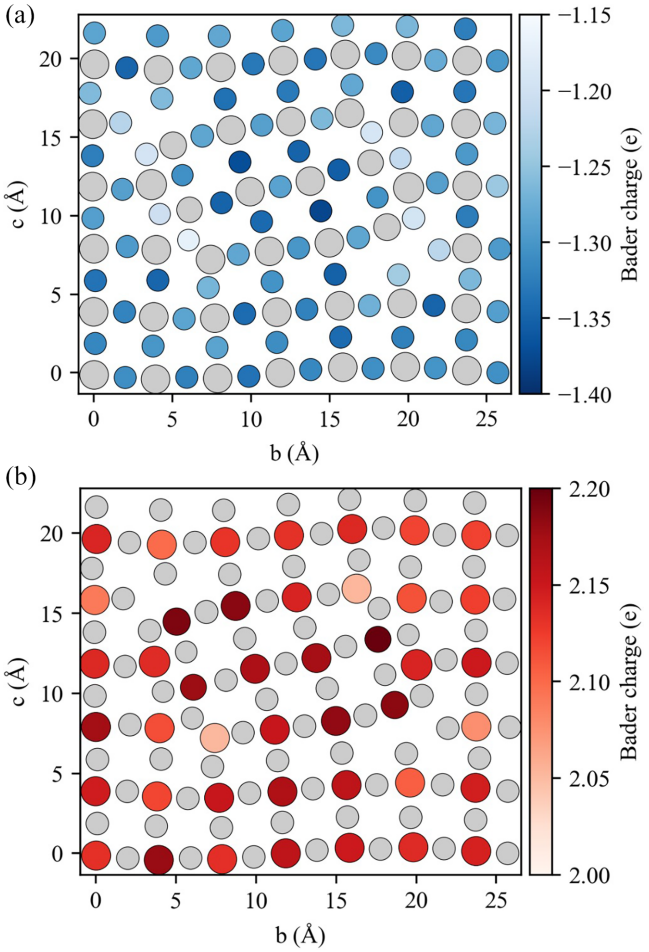


FIG. 8. Bader charges of the TiO_2-terminated dislocation with highlighted (a) oxygen and (b) titanium atoms.

interruption in the periodic lattice due to Bloch wave scattering at the dislocation core, leading to this spectral broadening [57]. This is consistent with the reduced band gap observed in the DOS. In addition, minor differences in spectral weight are observed between the two dislocations. The TiO_2-type dislocation seems to have a higher intensity of the valence and conduction bands, especially around the Γ point. Furthermore, the TiO_2-type dislocation shows stronger smearing compared to the SrO-type dislocation, indicating more scattering and therefore less mobile electrons.

Lastly, we analyze the charge distribution using Bader charges. For the SrO-type dislocation population, shown in Fig. 7, the oxygen atoms with the most negative charge, corresponding to the most reduced sites, are located directly along the dislocation cores, followed by atoms in the heavily distorted regions between them, consistent with previous DFT results [18]. A similar trend is observed for the titanium atoms. This indicates that electronic charge accumulates preferentially at the dislocation cores and, to a lesser extent, in the surrounding distorted lattice. In contrast, for the TiO_2-type dislocations, displayed in Fig. 8, the oxygen atoms at the dislocation core exhibit the least negative charge, indicating a more oxidized character, while those in the heavily distorted regions between dislocations are more negatively charged. For titanium, charge localization is more asymmetric. One titanium atom per dislocation core is more reduced, whereas the remaining titanium atoms in the core and in the distorted regions are comparatively more oxidized. Overall, these results show that charge accumulation can occur either directly at the dislocation core or within the surrounding distorted lattice, depending on the dislocation type.

IV. SUMMARY

In this work, we provided an overview of the structural and electrical properties of $SrTiO_3$, SrO-, and TiO_2-type dislocations. Regarding structural properties, SrO-type dislocations exhibit strain values up to 0.17, while TiO_2-type dislocations reach up to 0.13. This leads to localized polarization of up to 37 $\mu C/cm^2$ and 46 $\mu C/cm^2$, respectively, due to flexoelectricity. The symmetry breaking induced by dislocations introduces phonon modes between 600 cm^{-1} and 1000 cm^{-1} in both cases.

When investigating the electrical properties, dislocations reduce the bandgap from 2.27 eV for pristine bulk $SrTiO_3$ to 1.94 eV in the case of a SrO-type dislocation and 1.85 eV for a TiO_2-type dislocation. This is caused by smearing the oxygen $2p$ and titanium $3d$ states. The unfolded band structure revealed broadened bands, indicating increased scattering. SrO-type dislocations tend to show less broadening, inducing

less scattering and electrons with higher mobility. Lastly, a Bader charge analysis showed that charge carriers are mostly located either directly at the dislocation core or in the surrounding distorted lattice. Overall, these findings contribute to a deeper understanding of how dislocations influence the multifunctional properties of $SrTiO_3$ and related oxide materials and may guide the design of materials with tailored electronic and structural characteristics.

ACKNOWLEDGMENTS

The authors want to thank Calcul Québec and the Digital Research Alliance of Canada for providing support and computational resources for this work. A.R. gratefully acknowledges financial support through an NSERC discovery Grant No. (RGPIN-2024-06730). C.E.D. acknowledges support from the National Science Foundation under Grant No. DMR-2237674. The Flatiron Institute is a division of the Simons Foundation.

DATA AVAILABILITY

There are no publicly available research data or software supporting this manuscript. Requests for further information or data should be sent to the authors.

[1] D. de Ligny and P. Richet, High-temperature heat capacity and thermal expansion of $SrTiO_3$ and $SrZrO_3$ perovskites, Phys. Rev. B **53**, 3013 (1996).

[2] H. Weaver, Dielectric properties of single crystals of $SrTiO_3$ at low temperatures, J. Phys. Chem. Solids **11**, 274 (1959).

[3] J. Xu, Z. Zhu, H. Zhao, and Z. Luo, Metal-insulator-transition in $SrTiO_3$ induced by argon bombardment combined with field effect, AIP Adv. **4**, 127123 (2014).

[4] M. Wöhlecke, V. Marrello, and A. Onton, Refractive index of $BaTiO_3$ and $SrTiO_3$ films, J. Appl. Phys. **48**, 1748 (1977).

[5] J.-F. Ge, Z.-L. Liu, C. Liu, C.-L. Gao, D. Qian, Q.-K. Xue, Y. Liu, and J.-F. Jia, Superconductivity above 100 K in single-layer FeSe films on doped $SrTiO_3$, Nat. Mater. **14**, 285 (2015).

[6] J. H. Haeni, P. Irvin, W. Chang, R. Uecker, P. Reiche, Y. L. Li, S. Choudhury, W. Tian, M. E. Hawley, B. Craigo, A. K. Tagantsev, X. Q. Pan, S. K. Streiffer, L. Q. Chen, S. W. Kirchoefer, J. Levy, and D. G. Schlom, Room-temperature ferroelectricity in strained $SrTiO_3$, Nature (London) **430**, 758 (2004).

[7] M. Basini, M. Pancaldi, B. Wehinger, M. Udina, V. Unikandanunni, T. Tadano, M. C. Hoffmann, A. V. Balatsky, and S. Bonetti, Terahertz electric-field-driven dynamical multiferroicity in $SrTiO_3$, Nature (London) **628**, 534 (2024).

[8] E. B. Guedes, S. Muff, W. H. Brito, M. Caputo, H. Li, N. C. Plumb, J. H. Dil, and M. Radović, Universal structural influence on the 2D electron gas at $SrTiO_3$ surfaces, Adv. Sci. **8**, 2100602 (2021).

[9] C. Hou, W. Huang, W. Zhao, D. Zhang, Y. Yin, and X. Li, Ultrahigh energy density in $SrTiO_3$ film capacitors, ACS Appl. Mater. Interfaces **9**, 20484 (2017).

[10] S. Wu, L. Ren, J. Qing, F. Yu, K. Yang, M. Yang, Y. Wang, M. Meng, W. Zhou, X. Zhou, and S. Li, Bipolar resistance switching in transparent $ITO/LaAlO_3/SrTiO_3$ memristors, ACS Appl. Mater. Interfaces **6**, 8575 (2014).

[11] A. Rubano and D. Paparo, Optical second harmonic generation on $LaAlO_3/SrTiO_3$ interfaces: A review, Materials **16**, 4337 (2023).

[12] H. Lyu, T. Hisatomi, Y. Goto, M. Yoshida, T. Higashi, M. Katayama, T. Takata, T. Minegishi, H. Nishiyama, T. Yamada, Y. Sakata, K. Asakura, and K. Domen, An Al-doped $SrTiO_3$ photocatalyst maintaining sunlight-driven overall water splitting activity for over 1000 h of constant illumination, Chem. Sci. **10**, 3196 (2019).

[13] A. Bera, K. Wu, A. Sheikh, E. Alarousu, O. F. Mohammed, and T. Wu, Perovskite oxide $SrTiO_3$ as an efficient electron transporter for hybrid perovskite solar cells, J. Phys. Chem. C **118**, 28494 (2014).

[14] W. Sigle, C. Sarbu, D. Brunner, and M. Rühle, Dislocations in plastically deformed $SrTiO_3$, Philos. Mag. **86**, 4809 (2006).

[15] K. Szot, W. Speier, R. Carius, U. Zastrow, and W. Beyer, Localized metallic conductivity and self-healing during thermal reduction of $SrTiO_3$, Phys. Rev. Lett. **88**, 075508 (2002).

[16] A. H. Youssef, G. Kolhatkar, I. C. Amaechi, R. Katoch, Y. González, A. Merlen, and A. Ruediger, Giant step bunching on $SrTiO_3$ thin films grown epitaxially on vicinal MgO (100) surfaces, Appl. Surf. Sci. **570**, 151266 (2021).

[17] L. Porz, A. J. Klomp, X. Fang, N. Li, C. Yildirim, C. Detlefs, E. Bruder, M. Höfling, W. Rheinheimer, E. A. Patterson, P. Gao, K. Durst, A. Nakamura, K. Albe, H. Simons, and J. Rödel, Dislocation-toughened ceramics, Mater. Horiz. **8**, 1528 (2021).

[18] H. Chen, D. Yi, B. Xu, J. Ma, and C. Nan, Spontaneous symmetry breaking of dislocation core in $SrTiO_3$, Mater. Today Phys. **20**, 100453 (2021).

[19] P. Zubko, G. Catalan, A. Buckley, P. R. L. Welche, and J. F. Scott, Strain-gradient-induced polarization in $SrTiO_3$ single crystals, Phys. Rev. Lett. **99**, 167601 (2007).

[20] K. Szot, W. Speier, G. Bihlmayer, and R. Waser, Switching the electrical resistance of individual dislocations in single-crystalline $SrTiO_3$, Nat. Mater. **5**, 312 (2006).

[21] K. Szot, C. Rodenbücher, K. Rogacki, G. Bihlmayer, W. Speier, K. Roleder, F. Krok, H. Keller, A. Simon, and A. Bussmann-Holder, Transition to metallic and superconducting states induced by thermal or electrical deoxidation of the dislocation network in the surface region of $SrTiO_3$, Nanomaterials **14**, 1944 (2024).

[22] L. L. Rusevich, M. Tyunina, E. A. Kotomin, N. Nepomniashchaia, and A. Dejneka, The electronic properties of $SrTiO_{3-\delta}$ with oxygen vacancies or substitutions, Sci. Rep. **11**, 23341 (2021).

[23] X. Ran, Y. Bai, H. Zeng, J. Zhang, H. Fu, X. An, and X. Yang, Manipulating oxygen vacancy in $SrTiO_3$ nanoparticles to achieve enhanced photoelectrochemical performance in water splitting, ACS Appl. Nano Mater. **7**, 27543 (2024).

[24] D. A. Tenne, I. E. Gonenli, A. Soukiassian, D. G. Schlom, S. M. Nakhmanson, K. M. Rabe, and X. X. Xi, Raman study of

oxygen reduced and re-oxidized strontium titanate, Phys. Rev. B **76**, 024303 (2007).

[25] D. Marrocchelli, L. Sun, and B. Yildiz, Dislocations in $SrTiO_3$: Easy to reduce but not so fast for oxygen transport, J. Am. Chem. Soc. **137**, 4735 (2015).

[26] C. Rodenbücher, S. Menzel, D. Wrana, T. Gensch, C. Korte, F. Krok, and K. Szot, Current channeling along extended defects during electroreduction of $SrTiO_3$, Sci. Rep. **9**, 2502 (2019).

[27] J. Rakowsky and P. P. Dholabhai, Interface layer chemistry dependent oxygen defect formation in $BaZrO_3(110)/SrTiO_3(100)$ heterostructures, Energy Adv. **5**, 43 (2026).

[28] R. A. De Souza, Transport properties of dislocations in $SrTiO_3$ and other perovskites, Curr. Opin. Solid State Mater. Sci. **25**, 100923 (2021).

[29] S. P. Waldow and R. A. De Souza, Computational study of oxygen diffusion along a[100] dislocations in the perovskite oxide $SrTiO_3$, ACS Appl. Mater. Interfaces **8**, 12246 (2016).

[30] W. Ebmeyer, P. Hatton, B. P. Uberuaga, and P. P. Dholabhai, Influence of misfit dislocations on ionic conductivity at oxide interfaces, J. Mater. Chem. A **12**, 21252 (2024).

[31] H. Sha, Y. Ma, G. Cao, J. Cui, W. Yang, Q. Li, and R. Yu, Sub-nanometer-scale mapping of crystal orientation and depth-dependent structure of dislocation cores in $SrTiO_3$, Nat. Commun. **14**, 162 (2023).

[32] P. Gao, S. Yang, R. Ishikawa, N. Li, B. Feng, A. Kumamoto, N. Shibata, P. Yu, and Y. Ikuhara, Atomic-scale measurement of flexoelectric polarization at $SrTiO_3$ dislocations, Phys. Rev. Lett. **120**, 267601 (2018).

[33] M.-W. Chu, I. Szafraniak, R. Scholz, C. Harnagea, D. Hesse, M. Alexe, and U. Gösele, Impact of misfit dislocations on the polarization instability of epitaxial nanostructured ferroelectric perovskites, Nat. Mater. **3**, 87 (2004).

[34] T. Sumigawa, T. Shimada, K. Huang, Y. Mizuno, Y. Hagiwara, N. Ozaki, and T. Kitamura, Ultrasmall-scale brittle fracture initiated from a dislocation in $SrTiO_3$, Nano Lett. **22**, 2077 (2022).

[35] V. Nagarajan, C. L. Jia, H. Kohlstedt, R. Waser, I. B. Misirlioglu, S. P. Alpay, and R. Ramesh, Misfit dislocations in nanoscale ferroelectric heterostructures, Appl. Phys. Lett. **86**, 192910 (2005).

[36] C. Rodenbücher, G. Bihlmayer, C. Korte, and K. Szot, Gliding of conducting dislocations in $SrTiO_3$ at room temperature: Why oxygen vacancies are strongly bound to the cores of dislocations, APL Mater. **11**, 021108 (2023).

[37] X. Cheng, B. Wang, and L.-Q. Chen, Polarization near dislocation cores in $SrTiO_3$ single crystals: The role of flexoelectricity, Appl. Phys. Lett. **124**, 132905 (2024).

[38] M. L. D. Reis, P. Carrez, and P. Cordier, Interaction between dislocation and vacancies in magnesium oxide: Insights from atomistic simulations and elasticity theory, Phys. Rev. Mater. **5**, 063602 (2021).

[39] M. K. Nowotny, T. Bak, and J. Nowotny, Electrical properties and defect chemistry of TiO_2 single crystal. I. Electrical conductivity, J. Phys. Chem. B **110**, 16270 (2006).

[40] K. Otsuka, K. Matsunaga, A. Nakamura, S. Ii, A. Kuwabara, T. Yamamoto, and Y. Ikuhara, Effects of dislocations on the oxygen ionic conduction in yttria stabilized zirconia, Mater. Trans. **45**, 2042 (2004).

[41] L. Sun, D. Marrocchelli, and B. Yildiz, Edge dislocation slows down oxide ion diffusion in doped CeO_2 by segregation of charged defects, Nat. Commun. **6**, 6294 (2015).

[42] J. M. Soler, E. Artacho, J. D. Gale, A. García, J. Junquera, P. Ordejón, and D. Sánchez-Portal, The SIESTA method for *ab initio* order-N materials simulation, J. Phys.: Condens. Matter **14**, 2745 (2002).

[43] J. P. Perdew, K. Burke, and M. Ernzerhof, Generalized gradient approximation made simple, Phys. Rev. Lett. **77**, 3865 (1996).

[44] M. J. van Setten, M. Giantomassi, E. Bousquet, M. J. Verstraete, D. R. Hamann, X. Gonze, and G.-M. Rignanese, The PseudoDojo: Training and grading a 85 element optimized norm-conserving pseudopotential table, Comput. Phys. Commun. **226**, 39 (2018).

[45] H. J. Monkhorst and J. D. Pack, Special points for Brillouin-zone integrations, Phys. Rev. B **13**, 5188 (1976).

[46] V. Sharma, B. Bein, A. Lai, B. Pamuk, C. E. Dreyer, M. Fernández-Serra, and M. Dawber, Cooperative interactions between surface terminations explain photocatalytic water splitting activity on $SrTiO_3$, PRX Energy **1**, 023002 (2022).

[47] C. Ricca, I. Timrov, M. Cococcioni, N. Marzari, and U. Aschauer, Self-consistent DFT + U + V study of oxygen vacancies in $SrTiO_3$, Phys. Rev. Res. **2**, 023313 (2020).

[48] M. Schmidbauer, A. Kwasniewski, and J. Schwarzkopf, High-precision absolute lattice parameter determination of $SrTiO_3$, $DyScO_3$ and $NdGaO_3$ single crystals, Acta Cryst. B **68**, 8 (2012).

[49] S. F. Yuk, I. Sargin, N. Meyer, J. T. Krogel, S. P. Beckman, and V. R. Cooper, Putting error bars on density functional theory, Sci. Rep. **14**, 20219 (2024).

[50] K. Robinson, G. V. Gibbs, and P. H. Ribbe, Quadratic elongation: A quantitative measure of distortion in coordination polyhedra, Science **172**, 567 (1971).

[51] K. M. Rabe, M. Dawber, C. Lichtensteiger, C. H. Ahn, and J.-M. Triscone, Modern physics of ferroelectrics: Essential background, *Physics of Ferroelectrics*, Topics in Applied Physics Vol. 105 (Springer, Berlin, Heidelberg, 2007), pp. 1–30.

[52] V. Buscaglia, M. T. Buscaglia, and G. Canu, $BaTiO_3$-based ceramics: Fundamentals, properties and applications, *Encyclopedia of Materials: Technical Ceramics and Glasses* (Elsevier, 2021), pp. 311–344.

[53] G. Verbist, F. M. Peeters, and J. T. Devreese, Extended stability region for large bipolarons through interaction with multiple phonon branches, Ferroelectrics **130**, 27 (1992).

[54] K. van Benthem, C. Elsässer, and R. H. French, Bulk electronic structure of $SrTiO_3$: Experiment and theory, J. Appl. Phys. **90**, 6156 (2001).

[55] I. Derkaoui, M. Achehboune, R. I. Eglitis, A. I. Popov, I. Boukhoubza, M. A. B.-M. Kabatas, and A. Rezzouk, Influence of the Hubbard U correction on the electronic properties and chemical bands of the cubic ($Pm\bar{3}m$) phase of $SrTiO_3$ using GGA/PBE and LDA/CA-PZ approximations, Molecules **29**, 3081 (2024).

[56] S. G. Mayo, F. Yndurain, and J. M. Soler, Band unfolding made simple, J. Phys.: Condens. Matter **32**, 205902 (2020).

[57] J. Park, S. Huh, Y. W. Choi, D. Kang, M. Kim, D. Kim, S. Park, H. J. Choi, C. Kim, and Y. Yi, Visualizing the low-energy electronic structure of prototypical hybrid halide perovskite through clear band measurements, ACS Nano **18**, 7570 (2024).